Influence of Anisotropies on Transverse Modes in Oxide-Confined VCSELs

Pierluigi Debernardi, Gian Paolo Bava, Christian Degen, Ingo Fischer, and Wolfgang Elsäßer, *Senior Member, IEEE*

***Abstract*—We present a comprehensive fully vectorial model for the cavity eigenmodes of oxide-cofined vertical-cavity surface-emitting lasers (VCSELs) with the details of their complex structure. It includes device-inherent symmetry-breaking mechanisms like noncircular geometries and material anisotropies related to the elasto-optic and electro-optic effect. The latter is accounted for in the model starting from the material and doping profiles. We compare these theoretical results with experimental findings of spectrally and polarization-resolved transverse mode nearfields of oxide-confined VCSELs with two different aperture diameters. Within a parametric study of the influence of aperture anisotropies we are able to calculate frequencies and gains of all transverse mode families, their polarization dependence and their spatial mode profiles which are in good agreement with the experimental findings.**

***Index Terms*—Birefringence, polarization, symmetry-breaking, transverse modes, VCSEL, vectorial fields.**

I. Introduction

VERTICAL-CAVITY surface-emitting lasers (VCSELs) are attractive light sources for numerous technological applications due to their particular properties [1]. They exhibit good optical beam quality, 2-D array capabilities, high modulation frequencies, and the potential for cost-effective mass-production. The most highly developed VCSELs today are oxide-confined devices in which the aperture of a selectively oxidized layer in the top DBR-mirror provides transverse confinement for the injected carriers and the optical field [2]. As a result record low-threshold currents and high efficiencies have been achieved. The drawback of good transverse optical guiding is, however, the pronounced multimode emission already in comparably small devices. In general, a complicated transverse mode behavior seems to be typical for oxide-confined devices [3]. Consequently, considerable work has been carried out in order to identify the mechanisms that determine the transverse mode formation: interaction of cavity structure and gain medium [4], [5], induced birefringence [6]–[8], and noncircular oxide-windows [9] have been found to play important roles for the VCSELs' emission. However, up to now, a comprehensive analysis taking into account the interaction of all of these mechanisms is still missing due to the complexity of the problem.

In this paper, we present experimental investigations of the transverse mode formation in oxide-confined VCSELs with two exemplary aperture sizes. The VCSELs' emission is characterized by polarization and spectrally resolved nearfield measurements. Based on these experimental data, we present a detailed and rigorous vectorial VCSEL model. The problem of computing VCSEL's modes is quite tough, due to their complex structures and has been addressed by a variety of papers, with different degrees of approximation. Most of them rely on an approximate solution of the Helmholtz equation (see, for instance, the popular method proposed in [10]) that neglects the vectorial nature of the electromagnetic field. This can be a reasonable approximation in some cases; however, the rigorous vectorial approach is necessary to analyze the consequences of anisotropies on the polarization properties of VCSEL emission. They are important both for a better understanding of the basic physics [11] and also from the application point of view, where often a well-defined polarization is required. Even if some vectorial models for VCSELs have been proposed (see [12] for a review and a comparison between different models), our model offers for the first time the capability of including the effects of device inherent anisotropies in terms of field-induced birefringence and noncircular oxide-windows in a rigorous vectorial electromagnetic framework. The results of these modeling activities enable us to compare and evaluate the strength of the individual effects on the VCSEL's transverse mode characteristics and thus offer the perspective to improve the performance of future devices.

II. Experimental Results

The VCSELs under investigation are oxide-confined structures manufactured at the University of Ulm. Their structure is schematically depicted in Fig. 1 and described in more detail in [13]. Basically, they are AlGaAs-VCSELs with λ cavities operating around $\lambda = 810$ nm. The Bragg mirrors consist of AlGaAs $\lambda/4$ layers with different aluminum content and graded interfaces in terms of material composition. The so-called delta-doping technique is applied in the top mirror in order to reduce the average doping concentration [14], while the bottom mirror is homogeneously doped. The active region consists of three 8-nm GaAs QWs. The confinement of both the carriers and the optical field is achieved by means of a 30-nm-thick layer of oxidized AlAs in the first top-mirror layer (oxide refractive index of 1.6 [15]) with a central window of unoxidized material .

The optical power versus injection current characteristics (PI-curves) of two VCSELs with 6- and 11-μm oxide aperture diameter are depicted in Fig. 2. Threshold currents amount to

Manuscript received July 16, 2001. This work was supported by MADESS II (Progetto Finalizzato of Italian National Council of Research), the European Community Human Potential Research Training Network VISTA (HPRN-CT-2000-00034), and the Deutsche Forschungsgemeinschaft (within project EL 105/10).

P. Debernardi and G. P. Bava are with the IRITI-CNR, c/o Dipartimento di Elettronica, Politecnico di Torino, 10129 Torino, Italy, and also with the INFM, UdR Politecnico di Torino, 10129 Torino, Italy.

C. Degen, I. Fischer, and W. Elsäßer are with Institute of Applied Physics, Darmstadt University of Technology, 64289 Darmstadt, Germany.

Publisher Item Identifier S 0018-9197(02)00166-5.

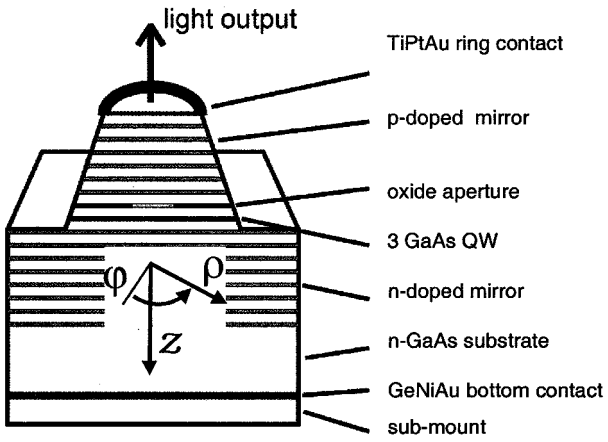

Fig. 1. Schematic of the VCSEL with the adopted cylindrical coordinate system.

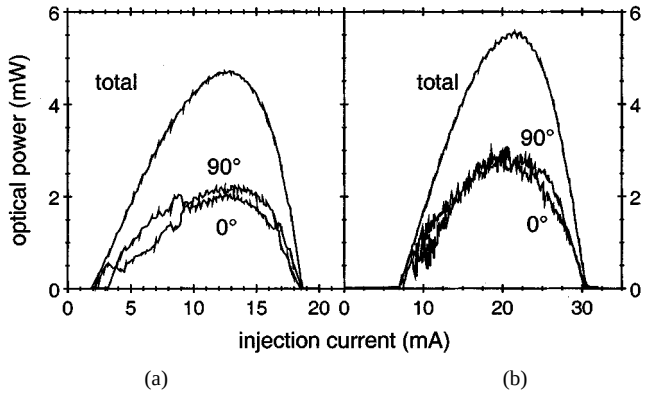

Fig. 2. Optical power versus injection current characteristics ("PI-curves") of VCSELs with (a) 6-μm and (b) 11-μm aperture diameter for the total power and the power fractions in orthogonal polarization directions "0°" and "90°."

$I_{th} = 2$ mA (6 μm device) and $I_{th} = 7$ mA (11 μm device) and the maximum output power is $P_{\max} = 4.8$ mW (6 μm device) and $P_{\max} = 5.9$ mW (11 μm device), respectively. The power in orthogonal polarization direction "0°" and "90°" is almost equally split. Both devices exhibit pronounced multi-transverse mode emission already at low injection currents.

In order to investigate the transverse modes properties, we have projected and magnified the top surface of the VCSELs onto a CCD-camera, i.e., we have recorded the intensity distribution in the laser near field. The results of these measurements are shown in Fig. 3 for the 6- and 11-μm VCSELs. Both VCSELs' nearfields are determined by superpositions of several modes. As a general feature, the nearfields in orthogonal polarization directions differ qualitatively: the 0° polarized parts of the nearfield in both lasers appear with a high degree of rotational symmetry at all injection currents, while the 90° polarized parts always possess a preferred direction as fixed by the orientation of strongly excited modes with only reflectional symmetry. This phenomenon has been conclusively described in [8] and has been attributed on a phenomenological level to a polarization-selective anisotropic optical guiding due to field-induced birefringence.

In order to clarify which particular modes contribute to the nearfields of the two VCSELs, we have spectrally resolved the nearfields by use of an imaging spectrometer and a CCD

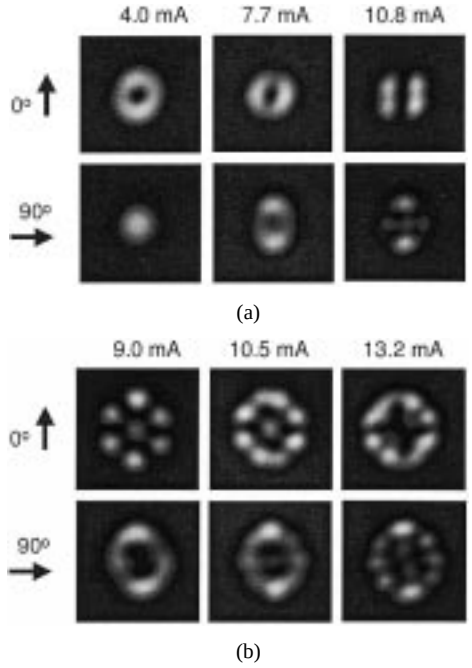

Fig. 3. Polarization-resolved nearfield images of the (a) 6-μm and (b) 11-μm VCSELs at injection currents as indicated.

camera. With this setup, the polarization-resolved nearfields are decomposed into their constituting transverse modes [8]. With this technique, we obtain images as depicted in Fig. 4. The modes are discriminated along the horizontal axis according to their spectral separation, while the fully 2-D resolution of the individual modes is preserved. The images have been recorded at the same injection currents as the images in the central column of Fig. 3 and, thus, can be directly compared. In this way it becomes obvious that the donut-shaped 0° polarized component of the 6-μm VCSEL's near field is a superposition of two orthogonally oriented first-order transverse modes, while the preferred direction in the 90° polarized part is determined by strongly excited first- and second-order modes, all vertically oriented and dominating other higher order modes [Fig. 4(a)]. The situation is similar for the 11-μm VCSEL's near fields as depicted in Fig. 4(b). The nearly circular shape of the 0° polarized near field at $I = 10.5$ mA originates from a superposition of several transverse modes of high azimuthal order (a third- and fourth-order mode are clearly visible in Fig. 4), while the elliptically distorted shape of the 90° polarized nearfield is caused by a mode with two bright vertically aligned lobes and weakly excited higher order modes, which are also aligned along the vertical direction. Moreover, the higher order modes in the 90° polarization deviate from the circular shape and exhibit a rather elliptical distortion.

To sum up the experimental findings, we have demonstrated that the emission of these VCSELs is divided into orthogonally polarized components of similar power. These components are determined by qualitatively different groups of transverse modes. The physical origin of the particular observed mode partition into orthogonal polarizations is probably related to birefringence as an inherent polarization effect, but also other anisotropies can possibly contribute. In the following part, we will present a vectorial model for the cavity eigenmodes

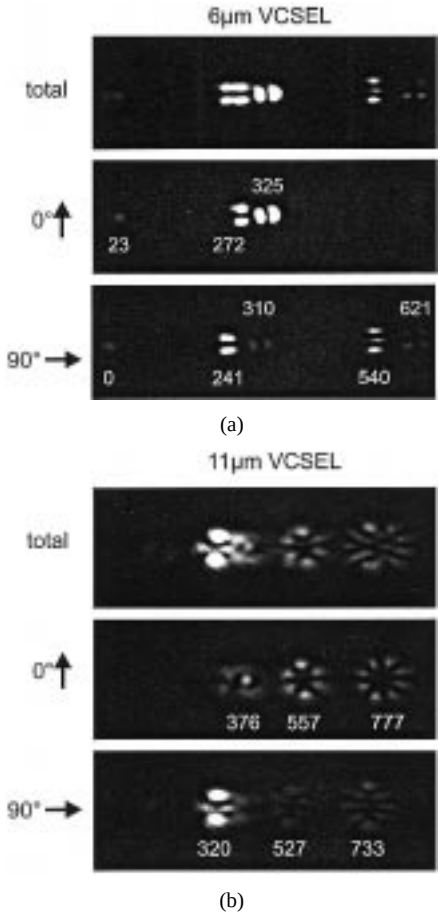

Fig. 4. Spectrally resolved nearfield images of the (a) 6 μm and (b) 11 μm VCSEL at $I_{inj} = 7.7$ and $I_{inj} = 10.5$ mA, respectively. The upper row contains the total nearfields, while the middle and lower rows are orthogonally polarized components of the total nearfields. The number indicate the mode spacing in Gigahertz, relative to the fundamental mode.

of VCSELs with complex transverse structure that includes different sources for device-inherent anisotropies and serves to evaluate their individual effects on the transverse mode formation.

III. VCSEL Model

The experimental results discussed above highlight the necessity of a fully vectorial model, capable of including both material anisotropies and noncircular symmetric geometries. Such features can be easily included in the calculation of the laser modes following the guidelines given in [9], recalled here for completeness. The stationary electromagnetic field is expanded on the complete and continuous basis of the TE and TM modes of an infinite reference medium

$$\begin{aligned}\mathbf{E}(\rho, \varphi, z) &= \sum_{\nu'} \int dk\, A_{\nu'}(z)\mathbf{E}_{\nu'}(\rho, \varphi) \\ &\simeq \sum_{\nu} A_{\nu}(z)\Delta k \mathbf{E}_{\nu}(\rho, \varphi) \end{aligned} \tag{1}$$

where the index ν labels the characteristics of the basis modes. They are classified according to the continuous radial component of the wavevector k, azimuthal variation, even or odd symmetry, TE or TM, forward and backward waves. Δk originates from approximating the integral over the continuous radial wavevector expansion by a finite sum of terms.

In each layer j of thickness L_j where the structure does not depend on the longitudinal coordinate z, the vector $\mathbf{A} = \{A_\nu \Delta k\}$ of mode amplitudes satisfies the coupled-mode equations

$$\frac{d\mathbf{A}}{dz} = (B + K_j \Delta k)\mathbf{A} \tag{2}$$

where B describes the free propagation in the reference material. It is a diagonal matrix of elements $(B)_{\nu\nu'} = -is_\alpha \beta_\nu \delta_{\nu\nu'}$, where $s_\alpha = \pm 1$ ($\alpha = f, b$ is an index which describes forward and backward propagation) and $\beta_\nu = \sqrt{k_r^2 - k^2}$ is the longitudinal wavevector component ($k_r = n_r \omega / c$, being n_r the refractive index of the reference material, ω the angular frequency, and c the velocity of light). The coupling between the modes is introduced by the nondiagonal matrix K, of elements [9]

$$\begin{aligned}(K)_{\nu\nu'} = &-\frac{i\omega}{C_\nu} \int_S dS \\ &\cdot \left\{ \mathbf{E}_{\nu t} \cdot \left[(\underline{\Delta\epsilon} \cdot \mathbf{E}_{\nu'})_t - \frac{(\underline{\Delta\epsilon}_{tz} \cdot \hat{z})\,(\underline{\Delta\epsilon} \cdot \mathbf{E}_{\nu'})_z}{\epsilon_r + \Delta\epsilon_{zz}} \right] \right. \\ &\left. + \frac{\epsilon_r E_{\nu z}}{\epsilon_r + \Delta\epsilon_{zz}} (\underline{\Delta\epsilon} \cdot \mathbf{E}_{\nu'})_z \right\} \end{aligned} \tag{3}$$

where the subscripts t and z indicate transverse and longitudinal components of the vectors, respectively, and C_ν is the power normalization constant. The tensor $\underline{\Delta\epsilon}$ describes the perturbation to the homogeneous and isotropic reference dielectric permittivity ϵ_r; its tensorial form accounts for the possibility of a nonisotropic perturbation related to the material anisotropy. The information on the device guiding geometry and dimensions is included in the model by defining, for each transversely inhomogeneous layer of the structure, the profile of the perturbation $\underline{\Delta\epsilon}(\rho, \varphi, z)$.

The solution of (2) can be expressed in the form of an exponential matrix and, hence, the mode amplitudes in each layer L_j are connected by

$$\mathbf{A}(z_{j+1}) = e^{(B + K_j \Delta k) L_j} \mathbf{A}(z_j) = T_j \mathbf{A}(z_j) \tag{4}$$

where the transmission matrix T_j has been introduced.

The closure of the problem is obtained by adding proper boundary conditions, i.e., the consistency of the forward and backward mode amplitudes at two reference interfaces. It is convenient to set these two sections to be the extreme lower ($z = L$) and upper ($z = 0$) layers, beyond which the structure does not present any transverse perturbation and the geometry is planar. With this choice, since the layers above (below) $z = 0$ ($z = L$) are multilayer stacks (or even a single medium), the chain matrix formalism can be applied to determine their reflectivity coefficient as a function of the wavevector k. The boundary conditions in these two sections explicitly read

$$\begin{aligned}\mathbf{A}^f(0) &= \Gamma_0 \mathbf{A}^b(0) \\ \mathbf{A}^b(L) &= \Gamma_L \mathbf{A}^f(L) \end{aligned} \tag{5}$$

where the diagonal matrices Γ_L and Γ_0 are the reflectivity coefficient components at the lower and upper interfaces, respectively.

By introducing the global transmission matrix $T = \prod_j T_j$ and considering explicitly its dependence on the index $\alpha = f, b$ (see [9] for further details), the boundary conditions (5) can be rewritten in the only unknown $\mathbf{A}^b(0)$

$$(T^{bf}\Gamma_L + T^{bb})\mathbf{A}^b(0) = \Gamma_0(T^{ff}\Gamma_L + T^{fb})\mathbf{A}^b(0) \quad (6)$$

which imposes the self consistency of backward and forward waves: a mode is then found when, after a complete round trip, the corresponding expansion coefficients exactly replicate themselves. This condition gives the frequency and the gain needed to fulfill the threshold condition of all the modes supported by the structure. Following the guidelines of [9, eq. (13)–(17)], (6) can be expressed as a standard eigenvalue problem for the wavelengths and gains, if one exploits the small (compared to the wavelength) active region thickness

$$\lambda\mathbf{A}^b(0) = M\mathbf{A}^b(0) \quad (7)$$

where $M = M_c^{-1}M_a$, which in turn are defined as

$$M_n = T_n^{bb} - \Gamma_0 T_n^{ff}\Gamma_L + T_n^{bf}\Gamma_L - \Gamma_0 T_n^{fb}, \qquad (n = c, a). \quad (8)$$

T_c and T_a are, respectively, the cold cavity and active contribution to the global transmission matrix

$$T = T_c + \lambda^{-1}T_a. \quad (9)$$

They stem from its linearization with respect to the unknown QW permittivity due to carriers ($\Delta\epsilon_a$). This is a good approximation, since the active thickness d is much smaller than the wavelength. The eigenvalue λ is then related to the active region permittivity by

$$\lambda^{-1} = -ik_r d\frac{\Delta\epsilon_a}{\epsilon_r}. \quad (10)$$

This relation links the eigenvalues to the active optical response and it allows for the threshold carrier density to be evaluated, once its effects on $\Delta\epsilon_a$ are known. However, since we are more interested in the basic understanding of the particular modal features observed experimentally, at this point we should clearly state that we will neither analyze the threshold carrier densities of the different modes nor pretend to go above threshold and then predict the modal power partition at the different injection currents. Instead, we think that by simply studying the conditions at threshold, we can obtain valuable informations as regards the modal shapes, polarizations and frequency positions. Therefore, in the following, we will focus mainly on the consequences of material anisotropies and of the deviations from circular transverse geometries.

IV. Symmetry-Breaking Mechanisms

In this section, we will focus on the symmetry-breaking mechanisms in the device. There are at least two possible main contributions, namely *noncircular transverse geometries* and *material anisotropies*, the latter having two different origins: the elasto-optic and the electro-optic effects. While in VCSELs the electro-optic effect is unavoidable due to their electrical pumping through the mirrors and can be evaluated starting from the characteristics of the device, the elasto-optic effect is less predictable and can have different sources. In ideal devices, there should be no strains in the structure; however, residual and unintentional strains can be due to some of the different fabrication steps and, maybe, to the mounting and packaging techniques. Moreover, strain distributions due to temperature gradients above threshold and to the oxide-layer shrinkage in oxide-confined devices could also play a role. An experimental investigation of a bunch of nominally identical devices was carried out in [16], where a spreading in the birefringence of the devices was found. Such behavior has been explained by the joint contributions of the electro-optic effect (which would give the mean value of the birefringence distribution) and the elasto-optic effect (related to its variance).

Clearly, in the model we account only for those contributions which are well defined and controlled, so in the following we will focus on the electro-optic and shape anisotropies.

A. Electro-Optic Effect

The material anisotropy can be represented by the impermeability tensor $\Delta\eta = \Delta(1/n^2)$ which, for the crystal group of interest ($\overline{4}3m$), in the contracted index notation is of the form [17]

$$\Delta(\eta)_i = r_{ij}\mathcal{E}_j \begin{cases} i = 1, 2 \ldots 6 \\ j = 1, 2, 3 \end{cases}, \qquad r = \begin{bmatrix} 0 & 0 & 0 \\ 0 & 0 & 0 \\ 0 & 0 & 0 \\ r_{41} & 0 & 0 \\ 0 & r_{41} & 0 \\ 0 & 0 & r_{41} \end{bmatrix} \quad (11)$$

where r_{41} is the corresponding coefficient for the electro-optic effect, and $\mathcal{E}_j$ is the dc electric field in the j direction (1, 2, 3 correspond to x, y, z orientations). In the case of interest here, the dc field is in the growth direction (which we will indicate as z); the induced anisotropy is then in the transverse plane xy and is represented by $\Delta\eta_6$. If one sets $(x, y) \equiv (110, [1-10])$ as a reference system, (i.e., the directions along which the chip is cleaved), a diagonal expression for the corresponding transverse dielectric permittivity is recovered as follows:

$$\underline{\Delta\epsilon}_t = \begin{bmatrix} \Delta\epsilon_{xx} & 0 \\ 0 & \Delta\epsilon_{yy} \end{bmatrix} \quad (12)$$

where

$$\Delta\epsilon_{xx}(\epsilon_{yy}) = +(-)n^4 r_{41}\mathcal{E}_z. \quad (13)$$

The static electric field $\mathcal{E}_z$ originates mainly from the doping needed in the mirrors to make the current flow at low voltages. The doping profile is a quite crucial point to obtain high wall-plug efficiencies and, therefore, it is the subject of intensive technological research [14]. The device under analysis uses the improved technology of a carbon δ-doped p-mirror. The determination of the dc field distribution requires the Poisson equation and the continuity equation for the current to be solved in a self-consistent way. This itself is a nontrivial problem which, in

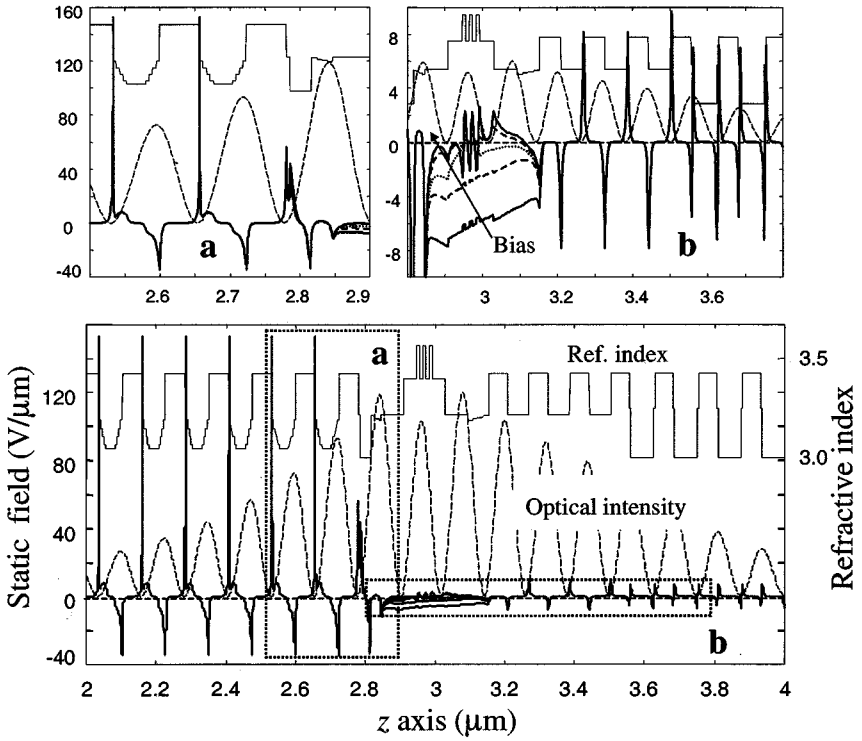

Fig. 5. Static field (left scale, thick lines), refractive index (right scale, thin line) and optical intensity (dashed line, arbitrary units) profiles for five values of applied bias: 0, 1, 1.5, 2, 2.5 V. The doping levels are: 2.5 10^{18} cm^{-3}C-doping with δ-doping at the heterointerfaces for the p-mirror and 2 10^{18} cm^{-3} Si-doping in the n-mirror. The regions **a** and **b** are shown in the enlargements on top.

turn, depends on a great number of parameters, that are in some cases not precisely known.

It is not the purpose of this work to go much inside transport models; a quite complete approach to treat carrier transport in VCSELs is presented, e.g., in [18] and we refer to it for the details. By applying this self-consistent model to our structure with δ-doping at the p-mirror hetero-interfaces in correspondence to field nodes, we obtain for the static electric field the result depicted in Fig. 5, where the longitudinal refractive index and corresponding optical intensity profile are also presented for reference. Many significant features can be observed: the static field distribution is a very rapidly varying function of position, which displays a multi-peaked behavior in the mirrors. This is related to the band-gap discontinuities and, therefore, it is qualitatively the same also with a constant doping concentration. Moreover, the field profile depends on the bias. The dependence is quite marginal in the mirrors and more effective in the cavity, where, however, it saturates rapidly toward small values. Finally, the effect of the delta-doping on the static field is local and located at optical intensity nodes as intended by this strategy.

B. Non-Circular Structures

It is well known that a circularly symmetric structure exhibits a mode degeneracy, i.e., it supports modes with different spatial distributions and polarizations with the same frequencies. The lifting of this degeneracy can be obtained by introducing a noncircular symmetry in the structure. In VCSELs, this property was already investigated experimentally by different groups (see, e.g., [19]–[22]) with interesting results. However, while within some technologies it seems easy to tailor the VCSEL's transverse shape (see, e.g., [21], where the result is obtained directly by photolithography), the situation is more complicated for the selectively wet-oxidized apertures. In fact, in these devices the shape of the oxide aperture strongly influences its electromagnetic properties and also defines the transverse current profile. If the oxidation speed were ideally isotropic, the aperture shape would be an exact replica of the mesa geometry. There are, however, many indications that the oxidation speed is not perfectly isotropic [2], [23]–[25], so that the final oxide aperture may differ from the mesa transverse geometry, which is circular in our sample and much larger than the oxide aperture.

Such an anisotropic oxidation speed seems to occur also in our device, as can be already seen from a first look at the spectrally resolved nearfield images (Fig. 4). They clearly present the typical characteristic of an oblong geometry in the y direction (0° in Figs. 3 and 4). With reference to the smaller oxide aperture device, the most relevant signatures of this fact are:

1) the two modes with the two spots oriented along y exhibit the lower frequencies;
2) the presence of a mode with three spots aligned along y axis.

In the following, we will focus on obtaining further information about the oxide aperture deformation by means of a parametric study of the mode distributions. For this aim, we have to first choose an adequate shape, capable of accounting both for the results of [2], [23], which indicate a higher oxidation speed in [100] with respect to [110] direction, and for the results published in [24], [25], which evidence an additional difference between [110] and [1$\bar{1}$0]. The former anisotropy results in a diamond shape with smoothed corners, while the latter introduces

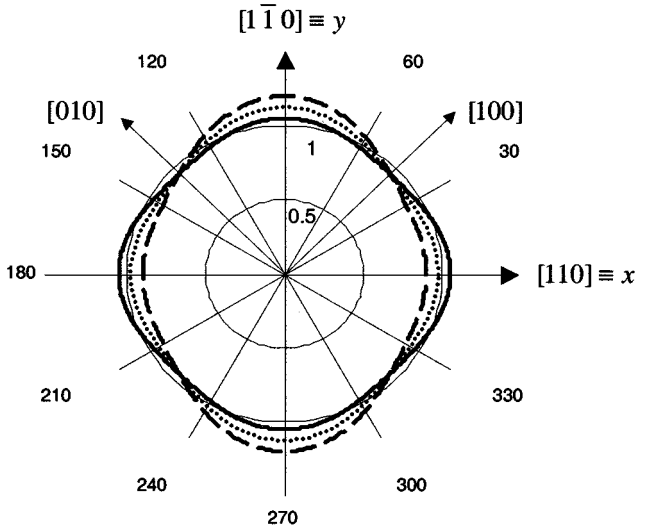

Fig. 6. Examples of possible shapes represented by (14); $\Delta_4 = 0.05$ and $\Delta_2 = 0, -7.5$ and -15% (continuous, dotted and dashed lines respectively).

an oblong deformation of such a diamond geometry. A possible analytical expression that includes all these features is

$$r(\varphi) = r_0(1 + \Delta_2 \cos(2\varphi) + \Delta_4 \cos(4\varphi)) \qquad (14)$$

where Δ_4 gives rise to the diamond shape for values in the range of 0%–6%, and Δ_2 controls the stretching. As an example, Fig. 6 depicts the curve (14) in polar coordinates for typical values of the two parameters.

V. Numerical Results

For circular structures without anisotropies, the different azimuthal modes are completely decoupled and one can solve the problem for a particular μ-value [see (A2) in Appendix A for the definition of μ] and find all the corresponding radial modes supported by the given structure. As already pointed out in [9], this fails if the angular rotational symmetry is broken or material anisotropies are included. However, in the present case, anisotropy and shape symmetry axes coincide and the geometry presents an even angular symmetry. As a consequence, even and odd azimuthal modes [l parameter in (A2)] are always decoupled. The same applies also to solutions with even and odd μ values, due to the even parity of the oxide-aperture shape. These considerations allow the reduction of the computational time by a factor of 16; the code to compute VCSEL's modes (that we call the VELM code) has been developed with Matlab and is run on a Pentium III, 400 MHz. To illustrate its numerical efficiency, we point out that the results presented in Fig. 8 have been computed in about 1-h CPU time.

As regards the electro-optic effect, we assume the corresponding anisotropy to be constant in the whole transverse sections, since the static electric field is mostly related to the doping profile and this does not exhibit transverse variations; in this case, the integral (A3) in Appendix A extends to infinity and gives a Dirac delta-function which selects only the diagonal terms in the κ_μ matrices. We discretize the longitudinal structure in different ways for the electromagnetic and

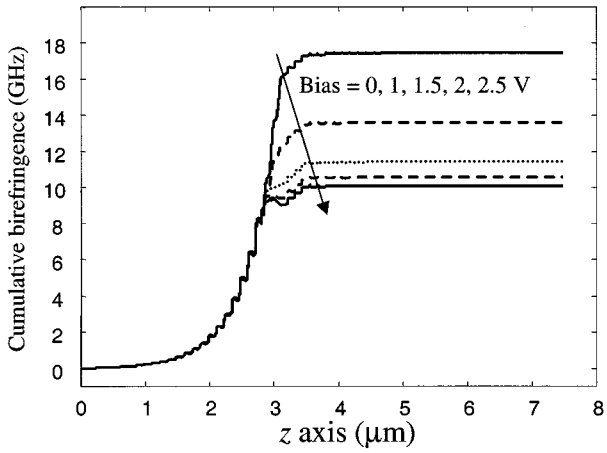

Fig. 7. Cumulative birefringence along the device corresponding to the static fields of Fig. 5. The origin of the z-axis is put at the interface between top mirror and air.

electrical problems in order to account for the strongly peaked longitudinal profile of the anisotropy corresponding to the static field of Fig. 5 with a reasonable computer effort. After having obtained the static field profile on a very dense longitudinal grid, we relax this discretization in the VELM-code by averaging the anisotropy in each L_j layer [see (4)]. In any case, the z-discretization represented by the L_j layers must be chosen so that the optical field can correctly feel the z-dependence of the anisotropy; therefore, they have to be much smaller than the optical wavelength. The longitudinal discretization accounts also for the graded index regions, that are fitted by a staircase approximation [see the refractive index profile in Fig. 5(a)].

In order to check that the VELM code works properly, we compute the birefringence on the fundamental mode in two different ways: first by applying our VELM code, and second by the simpler method proposed in [16]. By the latter method, the mode splitting is computed through perturbation theory, i.e., it evaluates the birefringence by means of the superposition of the normalized optical intensity and the induced anisotropy.

The corresponding results are presented in Fig. 7 for different biases. The graph represents the cumulative contributions along the device, and is, therefore, particularly suitable to put in evidence the regions where the effect is mostly located. The total birefringence accumulated in the device can be read from the value of the curves at the position of the end of the back mirror ($z = 7.5$ μm). The results are obtained by assuming $r_{41} = -1.6\ 10^{-12}$ V/m for GaAs and $-1.1\ 10^{-12}$ V/m for AlAs; the values for AlGaAs alloys are computed by linear interpolation of these two values [16], [26]. For our purposes, the representation of Fig. 7 is much more significant than the static field distribution of Fig. 5. In fact, it accounts for the interaction with the optical field which selects only the contributions from the negative peaks of the dc field [see Fig. 5(a)] in the p-mirror, while the overall contribution is more or less zero in the n-mirror [see Fig. 5(b)]. The birefringence is a function of the applied bias, but rapidly saturates above 1.5 V, as the static electric field in the cavity tends to be zero on average. Therefore, for bias values comparable to those of the experiment ($>$2 V above threshold), we obtain a birefringence value of about 10 GHz.

By applying the full VELM code, we find the same birefringence as results from the simpler method illustrated in Fig. 7, i.e., around 10 GHz at 2-V bias. However, this result does not perfectly match the measured birefringence of the fundamental mode of the smaller device, which is 23 GHz. There are many reasons for this discrepancy. First, the measured value accounts for all the phenomena that contribute to the lifting of the mode degeneracy and it is very difficult to experimentally separate the different contributions. However, the shape anisotropy of the fundamental mode is rather low for this relatively large device (computed by our model to be on the order of 1–2 GHz) and, thus there is still a difference of about 11–12 GHz between the experimental and theoretical results. The reasons for this larger material anisotropy can be manIfold. Among them:

1) underestimation of the static field profile, due to some parameters not adequate for the considered structure;
2) lack of knowledge of the exact values for r_{41} at 810 nm, especially for AlAs, for which the only result we found in the literature [26] is indirect;
3) presence of strain in the structure.

The latter effect represents probably the most important contribution to the difference between the computed (taking into account only the electro-optic contribution) and measured birefringence. This assumption is also strongly supported by other results [27], particularly by those published in [28], where a 50-GHz birefringence was measured on devices from Ulm University, similar to the ones under analysis.

Since it is difficult to infer which can be the origin of the strain in our structure, and in order to have consistency with the experiments, we magnify in the following calculations the electro-optic effect by a factor of 2.3 that recovers the experimentally determined birefringence values of about 23 GHz. This way of proceeding is similar to looking for an equivalent tensile strain that gives the missing 13 GHz with respect to the experiment, since the tensorial structure of the impermeability induced by the electro-optic effect is completely analogous [17], [29]. The next step comprises of a systematic study of the influence of oxide-aperture shape and dimensions on the modal properties of the device. The parameter Δ_4 that determines the diamond shape is fixed to 3% and is not varied. In fact, this is not too important since it does not introduce any "shape anisotropy," due to its angular symmetry, while the key parameter, with respect to this, is Δ_2. The results of such an analysis are presented in the following Figs. 8 and 9. In Fig. 8, we show the computed threshold gains for two devices with same shape but slightly different sizes. In analogy to LP notation, the modes are labeled by two numbers, and related to the azimuthal and radial variations of the strongest polarization component. However, since the structure is no longer circular, such a notation cannot always provide a precise description of the field profiles. These are depicted in Fig. 10.

The oxide-window shape adopted to compute the modes of Fig. 8 ($\Delta_2 = -10\%$ and $\Delta_4 = 3\%$) is obtained from the results shown in Fig. 9 where, for $r_0 = 2.5$ μm, we varied the stretching of the oxide aperture. To enable a detailed analysis, we show magnified views of the mode positions in the detuning-gain plane, by taking Δ_2 as a parameter. Since, in the measurements, all the modes of the family (1,1) are visible, we report these solutions in a larger expansion at the bottom of the

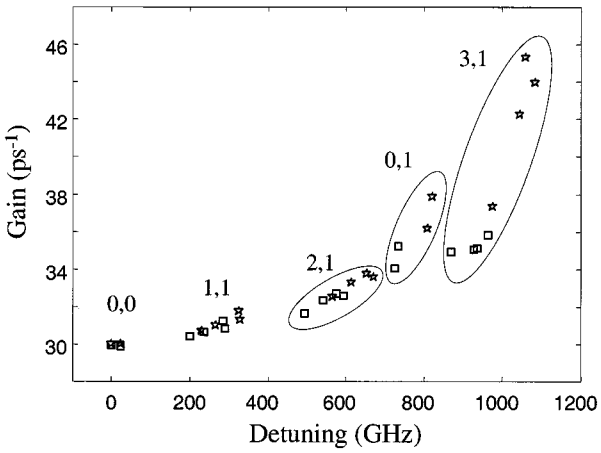

Fig. 8. Lower order mode gain versus frequency, with respect to the fundamental modes for two structures with the same oxide shape ($\Delta_2 = -10\%$ and $\Delta_4 = 3\%$) but different size r_0 [see (14)]. The squares refer to $r_0 = 2.7$ μm while the stars refers to $r_0 = 2.5$ μm. The pair of numbers indicate the mode family.

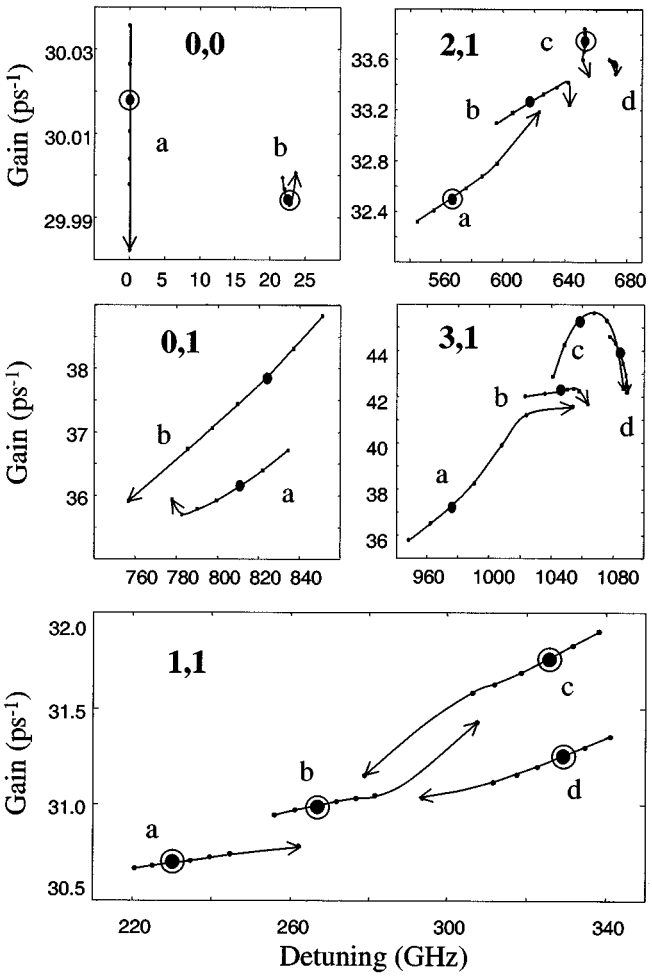

Fig. 9. Lower order mode distribution in the gain-detuning plane for structures with the same oxide size ($r_0 = 2.5$ μm and $\Delta_4 = 3\%$) but different stretchings ($\Delta_2 = -13, -11.5, -10, -8.5, -7, -5, 0\%$. The arrows point toward the $\Delta_2 = 0\%$ case). The solutions with $\Delta_2 = -10\%$ best fit the measurements and are shown by magnified symbols. The circles evidence the modes observed in the experiment.

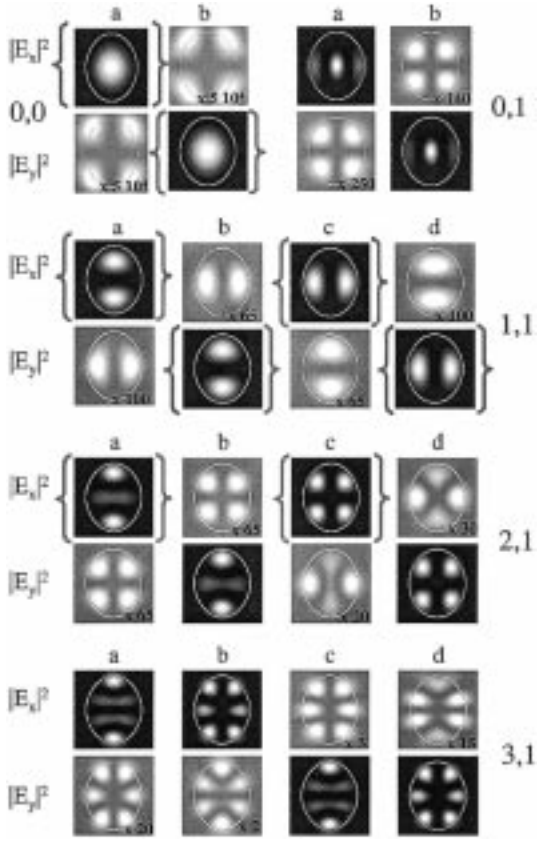

Fig. 10. Polarization-resolved output field profiles for the modes of Fig. 8. For reference, the oxide window is also depicted. The letters follow the frequency order; gray brackets evidence the experimentally observed modes.

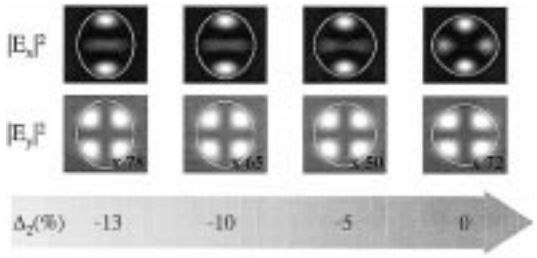

Fig. 11. Polarization-resolved output field profiles for modes (2,1,a) of Fig. 9 for different oxide-aperture shapes.

figure. Concentrating attention on these modes and comparing theoretical and experimental results, it turns out that good agreement is found for $\Delta_2 = -10\%$. This value corresponds to a 20% axis ratio, in surprisingly good agreement with [24], where by means of a simple parametric study of a rectangular waveguide a 3.3×4 μm-wide aperture was estimated. Moreover, it is worth noting that a structure without any stretching (i.e., $\Delta_2 = 0$, which correspond to the arrow points) does not provide the correct correspondence between the modes (1,1) in the experiment and their frequency positions. This is quite evident if one compares Fig. 4(a) with Figs. 9 and 10).

Beside the (1,1) family, Fig. 10 also depicts all the other modes evidenced by the bold bullets of Fig. 9. They are grouped on the basis of the membership to the same family (i.e., the same i, j indices). Except for the modes $(0, j)$ displayed on top, four solutions exist in each family and are labeled by the letters a, b, c, d following their proper frequency order. They correspond to the different azimuthal variations (index $l =$ even or odd) in the two possible polarizations. Each mode is by definition characterized by three components, of which we give only x and y (the longitudinal component E_z, which is the smallest, is here omitted since its intensity is always negligible for our purposes). In Fig. 10, the minor transverse field component has been evidenced by a lighter background and amplified by the factor which appears in the inset. Such a minor component is observable only in small devices and it is here reported for completeness and to emphasize the vectorial nature of the computed optical fields. Furthermore, this representation should clarify that, strictly speaking, the polarization in VCSELs is never linear. This aspect has been analyzed in [30], where the four lobed distribution of the minor component of the fundamental mode was experimentally observed. However, since in most devices the ratio between transverse mode components is always rather high, it is commonly accepted to have field "polarized" along a certain direction in that sense that the main component is addressed.

As already stated, the analysis is based on modes at threshold, so we are not able to predict exactly which are the lasing modes and how the power is partitioned among them. Nethertheless, such an analysis is sufficient to reproduce quite precisely the modal shapes, frequencies and, to a good extent, the favored mode within a certain family. This can be clearly seen if one compares the polarization-resolved experimental and theoretical results in two representative cases.

- Modes (1,1) display the correct frequency positions, polarization and spatial profiles and, moreover, mode (1,1,c) that theoretically requires a higher threshold gain, also in the experiment displays a lower power.
- In the family (2,1), the lowest gain mode is the mode (2,1,a) and this is also the one with the highest detected power in the corresponding frequency region. Moreover, the other detected mode (2,1,c) also has the correct profile, polarization, and frequency position.

With respect to the mode (2,1,a), characterized by an unusual three-spot spatial distribution, it is interesting to consider the results presented in Fig. 11. They show the effect of the oxide aperture shape on the corresponding modal profile, which mainly motivated us to look for an influence of the anisotropy of the oxidation speed. These results show very clearly the influence of the oblong shape on the modal profile: for a device with a shape without any direction preference we recover, even with material anisotropies, what we expect from a (2,1) mode, i.e., a four-spot distribution. The material anisotropy in this case acts to fix the polarization, since in ideally circular structures without anisotropies, the power is nearly equally shared by the two transverse components [29]. A stretching of the symmetric shape pushes more and more together the two spots aligned along the shorter side, ending up with a three-spot distribution for axis ratios exceeding 15%–20%. The presence of an oblong oxide-window has now gained a strong validation both from the frequency distribution of the mode family (1,1) and from the

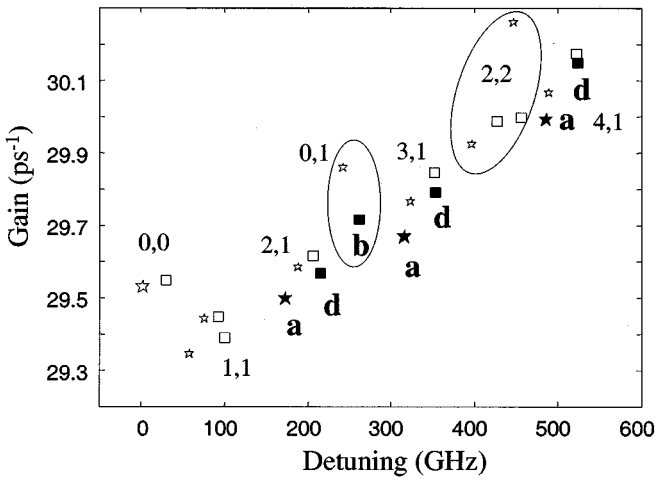

Fig. 12. As in Fig. 8 but for the larger device ($r_0 = 5.5\ \mu$m). Squares (stars) refer to fields with a dominating x (y) polarization; only the modes detected in the experiment are labeled by letters and denoted by full symbols.

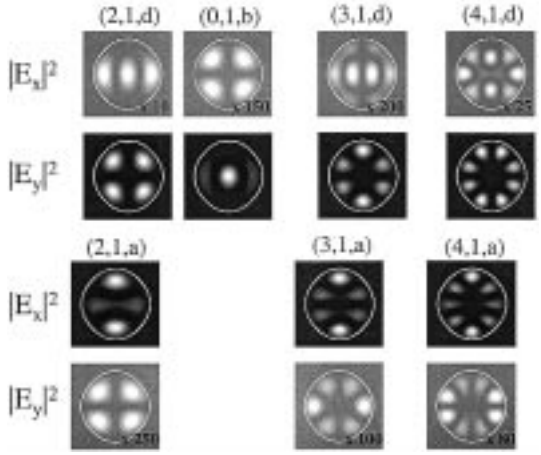

Fig. 13. Polarization-resolved field profiles corresponding to the modes indicated by the letters in Fig. 12

field profile of mode (2,1,a); our parametric study allows one to quantify such a deformation of $\Delta_2 = -10\%$ that simultaneously gives all the features detected in the experiment.

As a further demonstration that the parameters we obtained are consistent, we considered the larger aperture device and computed the lower order modes gains and frequencies (Fig. 12) and profiles (Fig. 13). According to the interpretation of the origin of the noncircular aperture shape, we scaled the values of $\Delta_{2,4}$ to account for the fact that the effect of the anisotropic oxidation speed is inversely proportional to the diameter of the final aperture. In Fig. 12, the letters label only the observed modes, which are depicted in Fig. 13. In this case, we get a good matching between theory and experiment with respect to the modal profiles; the corresponding detunings reported in Fig. 12 are, however, slightly mismatched, even if the polarization splittings fit well. This fact can have many causes, among which we recall the less precise measurement of the fundamental mode frequency (since this mode is highly suppressed) and a possible deviation from the nominal oxide-aperture size. Some influence can originate also from the combined role of thermal and carrier effects. Nevertheless, most of the characteristics are also reproduced in this case. The dominant mode in the experiment is now the mode (2,1,a), whose spatial distribution is quite different compared to the one in the smaller aperture device. This is related to the reduced (but still effective) influence of the anisotropic oxidation speed, responsible for the preference of field distributions peaked along the longer axis.

Finally, it is interesting to compare the consequences of material anisotropy and noncircular oxide window shape from a general viewpoint. We find that it is difficult to draw a conclusion valid for all the modes. In fact the shape anisotropy has different influence on different modes, see e.g., the modes (0,0) and (1,1) of Fig. 9, where in the first case, the dominant effect is the material anisotropy, while in the latter, the shape anisotropy dominates by far. Nevertheless, as a general feature of material anisotropy, the presence of two directions with a higher and lower refractive indices induces a splitting of the modes in the different families, where the lower frequency modes always have their major field component oriented in the direction of the higher refractive index.

VI. Conclusion

A detailed joint experimental and theoretical analysis of transverse modes in oxide-confined VCSELs has been carried out. The experimentally detected mode profiles and frequencies of two multimode devices with different sizes show clear evidence of both material and shape anisotropies in the devices. In order to rigorously handle these effects, we presented a numerically efficient vectorial model that, starting from the basic structural design of the devices, is capable, for the first time, to include on the same level all the relevant anisotropies in VCSEL devices and then to make possible detailed comparisons with the experiments. As a result, our treatment serves to distinguish the individual signatures of the two effects in the mode profiles and their frequency spacings found in the experiment. A parametric study of the 6-μm device concentrating on the effects of a noncircular oxide-window, due to the nonisotropic oxidation speed, results in estimation of 20% deformation with respect to the circular aperture device. The use of this deduced shape allows the experimental results for the larger device also to be reproduced. In both cases, the joint effect of shape anisotropy and electro-optic effect due to hetero-interfaces and doping -profiles underestimate the amount of measured birefringence by about 10 GHz. Thus, our analysis evidences that the electro-optic effect can hardly explain the measured birefringence and our results give valuable indications for a contribution also from the elasto-optic effect.

The excellent agreement obtained between experimental and theoretical modal frequencies, gains, and spatial mode profiles can be considered as a conclusive proof that vectorial models are required in order to describe VCSEL's modes with high reliability and, thus, to possibly improve the understanding and performance of future devices.

Appendix A
Coupling Coefficients for Material Anisotropy

The coupling coefficient in presence of material anisotropies can be computed by means of (4) and (12) and by writing the

TABLE I
STRUCTURE OF THE COUPLING COEFFICIENT MATRIX

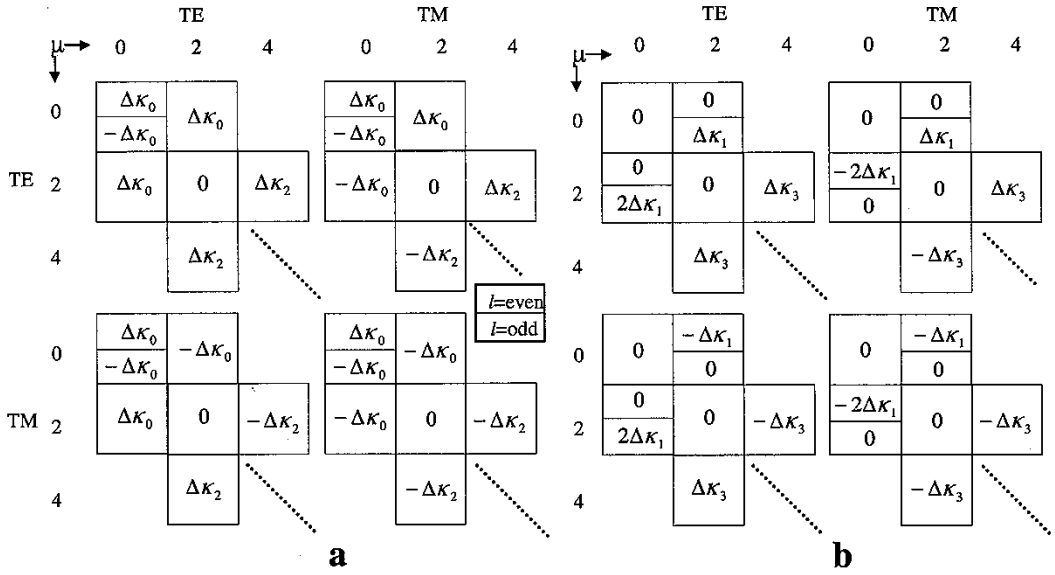

mode basis (in [9, A1]) in Cartesian components. In this way, one gets [29]

$$(K_t^{ff})_{\mu\mu'} = -\frac{i\omega}{C_\mu}\int_S dS\{\Delta\epsilon_{xx}(J_{\mu_+}f_{\mu_+} + s_p J_{\mu_-}f_{\mu_-}) \cdot (J_{\mu'_+}f_{\mu'_+} + s_p J_{\mu'_-}f_{\mu'_-}) + \Delta\epsilon_{yy}(J_{\mu_+}g_{\mu_+} + s_p J_{\mu_-}g_{\mu_-}) \cdot (J_{\mu'_+}g_{\mu'_+} + s_p J_{\mu'_-}g_{\mu'_-})\} \quad \text{(A1)}$$

where the compact notations $J_{\mu_\pm}f_{\mu_\pm} = J_{\mu\pm1}(k\rho)f_{\mu_{\pm1}}$ and $J_{\mu'_\pm}f_{\mu'_\pm} = J_{\mu'\pm1}(k'\rho)f_{\mu'\pm1}$ have been introduced, $s_p = \pm1$ for TE and TM modes and the azimuthal dependence are given by

$$f_{\mu l}(\varphi),\, g_{\mu l}(\varphi) = \begin{cases} \cos(\mu\varphi),\, -\sin(\mu\varphi) & l = \text{even} \\ \sin(\mu\varphi),\, +\cos(\mu\varphi) & l = \text{odd}. \end{cases} \quad \text{(A2)}$$

It follows that the coupling coefficients related to the anisotropy, apart from the common term $-i\omega Z^p k/2$ (see [9, (A5)]), have the form illustrated in Table I, where we have set $\Delta = \Delta\epsilon_{xx} - \Delta\epsilon_{yy}$ and the submatrices κ_μ are defined by

$$\kappa_\mu(k, k') = \int_\rho J_{\mu+1}(k\rho)J_{\mu+1}(k'\rho)\rho\, d\rho. \quad \text{(A3)}$$

The anisotropy couples neighbor modes of the same azimuthal parity μ in a sort of a banded arrangement (see the structure in the Table). For modes with $\mu = 1, 3, \ldots$ the matrix structure of Table I(a) holds, while Table I(b) refers to $\mu = 0, 2, \ldots$. The differences in the corresponding matrix structures arise from the peculiarities of modes $\mu = 0, 1$ and are, therefore, related to the upper left corners of the four submatrices in the tables (which account for TE–TM couplings). Conversely, all the modes in the basis with $\mu > 1$ are instead insensitive to azimuthal spatial variations (A2).

APPENDIX B
COUPLING COEFFICIENTS FOR NON-CIRCULAR TRANSVERSE GEOMETRIES

The guidelines to compute the coupling coefficient in the presence of noncircular structures are presented in [9, Appendix] to which we refer for more details. There, explicit expressions are given for an elliptical geometry. In the present case, we have to consider the shape given by (14) and follow the same steps of [9], which we recall here for completeness. The surface integral (4) to compute the coupling coefficient elements is, in this case, related to the perturbation $\Delta\epsilon$ [defined on the area specified by $r(\varphi)$] and is more conveniently rewritten as

$$(K_t^{ff})_{\mu\mu'} = -\frac{i\omega}{C_\mu}\Delta\epsilon \times \left\{\int_0^{2\pi}\mathcal{F}(\varphi)\,d\varphi\int_0^{r(\varphi)}\rho\,d\rho(s_p J_{\mu_+} + J_{\mu_-}) \cdot (s_{p'}J_{\mu'_+} + J_{\mu'_-}) + \int_0^{2\pi}\mathcal{G}(\varphi)\,d\varphi\int_0^{r(\varphi)}\rho\,d\rho \cdot (J_{\mu_-} - s_p J_{\mu_+})(J_{\mu'_-} - s_{p'}J_{\mu'_+})\right\} \quad \text{(B1)}$$

where we set $\mathcal{F}(\mathcal{G}) = f_{\mu l}f_{\mu' l'}(g_{\mu l}g_{\mu' l'})$ and we used the same notations of (A1). The preceding integral is efficiently evaluated by first analytically integrating over the angular variable. Only the last integration over the radial coordinate must be carried out numerically, i.e.

$$\int_0^{2\pi}d\varphi\int_0^{r(\varphi)}\mathcal{R}(\rho)\mathcal{F}(\varphi)\rho\,d\rho = \int_0^{r_{\max}}\mathcal{R}(\rho)\Psi_{\mu\mu'}(\rho)\rho\,d\rho. \quad \text{(B2)}$$

$\mathcal{R}(\rho)$ is related to Bessel functions through the preceding equation while Ψ is the angular integration of $\mathcal{F}(\mathcal{G})$

$$\Psi_{\mu\mu'}(\rho) = \int_{\overline{\varphi}_i(\rho)} \mathcal{F}(\mathcal{G})\, d\varphi = [\psi_{\mu-\mu'}(\rho) \pm s_l \psi_{\mu+\mu'}(\rho)]\ \delta_{ll'} \tag{B3}$$

where the $\pm$ refers to $\mathcal{F}/\mathcal{G}$, $s_l = 1/-1$ ($l =$ even/odd) and

$$\psi_{\mu\pm\mu'}(\rho) = \int_{\overline{\varphi}_i(\rho)} \cos((\mu \pm \mu')\varphi)\, d\varphi. \tag{B4}$$

The angular domain of integration $\overline{\varphi}_i(\rho)$ is obtained by inverting the relation $r(\varphi)$. For example, in the interval $[0, \pi/2]$, we obtain

$$\overline{\varphi}_i(\rho) = \begin{cases} 0, \pi/2 & 0 < \rho < r_{\min} \\ \cos^{-1}\Theta_i & r_{\min} < \rho < r_{\max} \end{cases} \tag{B5}$$

which represents a continuous angular domain in the inner region and a piecewise, ρ-dependent domain in the outer part, where the integration limits are obtained by

$$\Theta_i = \frac{1}{2}\sqrt{1 - \frac{\Delta_2}{2\Delta_4} \pm \sqrt{\frac{\Delta_4 + r/r_0 - 1}{2\Delta_4} + \frac{\Delta_2^2}{2\Delta_4^2}}}\,. \tag{B6}$$

The preceding relation gives one or two solutions, depending on the parameters (only values with $|\Theta_i| <= 1$ must be considered).

The coupling of modes with different μ occurs in the outer region, since $\Psi = \Psi_{\mu\mu'}(\rho)\delta_{\mu\mu'}$ for $\rho < r_{\min}$. Moreover, due to the even angular symmetry of the oxide aperture, (B4) differs from zero only when $\mu \pm \mu'$ is an even number. That is, the system couples only the modes with same azimuthal parity; similarly modes with different angular variation l are completely decoupled. These features, which stem from the even periodicity of the geometry under analysis, reduce the numerical complexity of the problem, allowing separate eigenvalue problems of lower order to be solved.

ACKNOWLEDGMENT

The authors would like to thank Prof. K. J. Ebeling and his team (University of Ulm) for providing the excellently suited laser structures.

REFERENCES

[1] K. J. Ebeling, U. Fiedler, G. Reiner, and B. Weigl, "Efficient vertical cavity surface emitting laser diodes for high bit rate optical data transmission," *AEU Int. J. Electron. Commun.*, vol. 50, pp. 316–326, 1996.

[2] D. L. Huffaker, D. G. Deppe, and K. Kumar, "Native-oxide defined ring contact for low threshold vertical-cavity laser," *Appl. Phys. Lett.*, vol. 65, p. 97, 1994.

[3] C. Degen, I. Fischer, and W. Elsäßer, "Transverse modes in oxide confined VCSELs: Influence of pump profile, spatial hole burning, and thermal effects," *Opt. Exp.*, vol. 5, pp. 38–47, 1999.

[4] S. P. Hegarty, G. Huyet, P. Porta, J. G. McInerney, K. D. Choquette, K. M. Geib, and H. Q. Hou, "Transverse-mode structure and pattern formation in oxide-confined vertical-cavity semiconductor lasers," *J. Opt. Soc. Amer. B*, vol. 16, pp. 2060–2071, 1999.

[5] C. Degen, I. Fischer, W. Elsäßer, L. Fratta, P. Debernardi, G. P. Bava, M. Brunner, R. Hövel, M. Moser, and K. Gulden, "Transverse modes in thermally detuned oxide confined vertical-cavity surface-emitting lasers," *Phys. Rev. A*, vol. 63, p. 023 817, 2001.

[6] M. Travagnin, M. P. van Exter, A. K. Jansen van Doorn, and J. P. Woerdman, "Role of optical anisotropies in the polarization properties of surface-emitting semiconductor lasers," *Phys. Rev. A*, vol. 54, pp. 1647–1660, 1996.

[7] A. Valle, K. A. Shore, and L. Pesquera, "Polarization selection in Birefringent vertical-cavity surface emitting lasers," *IEEE J. Lightwave Technol.*, vol. 14, pp. 2062–2068, 1996.

[8] C. Degen, B. Krauskopf, G. Jennemann, I. Fischer, and W. Elsäßer, "Polarization selective symmetry breaking in the near-fields of vertical cavity surface emitting lasers," *J. Opt. B: Quantum Semiclass. Opt.*, vol. 2, pp. 517–525, 2000.

[9] G. P. Bava, P. Debernardi, and L. Fratta, "Three-dimensional model for vectorial fields in vertical-cavity surface-emitting lasers," *Phys. Rev. A*, vol. 63, p. 23 816, 2001.

[10] G. R. Hadley, "Effective index model for vertical cavity lasers," *Opt. Lett.*, vol. 20, p. 1483, 1995.

[11] M. San Miguel, Q. Feng, and J. V. Moloney, "Light-polarization dynamics in surface-emitting semiconductor laser," *Phys. Rev. A*, vol. 52, p. 1728, 1995.

[12] P. Bienstman, R. Baets, J. Vukusic, A. Larsson, M. Noble, M. Brunner, K. Gulden, P. Debernardi, L. Fratta, G. P. Bava, H. Wenzel, B. Klein, O. Conradi, R. Pregla, S. Riyopoulos, J.-F. P. Seurin, and S. L. Chuang, "Comparison of optical VCSEL models on the simulation of oxide-confined devices," *IEEE J. Quantum Electron.*, vol. 37, pp. 1618–1631, Dec. 2001.

[13] R. Jäger, M. Grabherr, C. Jung, R. Michalzik, G. Reiner, B. Weigl, and K. J. Ebeling, "57% wallplug efficiency oxide-confined 850 nm wavelength GaAs VCSELs," *Electron. Lett.*, vol. 33, pp. 1790–1791, 1997.

[14] G. Reiner, E. Zeeb, B. Möller, M. Ries, and K. J. Ebeling, "Optimization of planar Be-doped InGaAs VCSEL's with two-sided output," *IEEE Photon. Technol. Lett.*, vol. 7, pp. 730–732, 1995.

[15] T. R. Nelson, Jr., J. P. Prineas, G. Khitrova, H. M. Gibbs, J. D. Berger, and E. K. Lindmark, "Room-temperature normal-mode coupling in a semiconductor microcavity utilizing native-oxide AlAs/GaAs mirrors," *Appl. Phys. Lett.*, vol. 69, p. 3031, 1996.

[16] M. P. van Exter, A. K. Jansen van Doorn, and J. P. Woerdman, "Electro-optic effect and birefringence in semiconductor vertical-cavity lasers," *Phys. Rev. A*, vol. 56, p. 845, 1997.

[17] A. Yariv and P. Yeh, *Optical Waves in Crystals*. New York: Wiley, 1984, ch. 7.

[18] D. W. Winston and R. E. Hayes, "Optoelectronic device simulation of Bragg reflectors and their Influence on surface-emitting lasers characteristics," *IEEE J. Quantum Electron.*, vol. 34, p. 707, 1998.

[19] K. D. Choquette and R. Leibenguth, "Control of vertical cavity laser polarization with anisotropic transverse cavities," *IEEE Photon. Technol. Lett.*, vol. 6, p. 40, 1994.

[20] G. Vershafelt, M. vander Vleuten, M. Creusenm, E. Smalbrugge, T. G. van de Roer, F. Karouta, R. C. Strijbos, J. Dankaert, I. Veretennicoff, B. Ryvkin, H. Thiepont, and G. A. Acket, "Polarization stabilization in vertical cavity surface emitting lasers through asymmetric current injection," *IEEE Photon. Technol. Lett.*, vol. 12, p. 945, 2000.

[21] M. Ortsiefer, R. Shau, M. Zigldrum, G. Böhm, F. Köhler, and M. C. Amann, "Submilliamp long-wavelength InP-based vertical-cavity surface-emitting lasers with stable polarization," *Electron. Lett.*, vol. 36, p. 1124, 2000.

[22] N. Uekiu, H. Nakayama, J. Sakurai, A. Murakami, H. Otoma, Y. Miyamoto, M. Yamamoto, R. Ishii, M. Yoshikawa, and T. Nakamura, "Complete polarization control of 12*8-bit matrix-addressed oxide-confined vertical-cavity surface-emitting laser array," *Jpn. J. Appl. Phys., Pt. 2 (Letters)*, vol. 12, p. 33, 2001.

[23] K. D. Choquette, K. M. Geib, H. C. Chui, B. E. Hammons, H. Q. Hou, and T. J. Drummond, "Selective oxidation of buried AlGaAs versus AlAs layers," *Appl. Phys. Lett.*, vol. 69, p. 1385, 1996.

[24] K. Lear, K. D. Choquette, P. R. Schneider, Jr., and S. P. Kilcoyne, "Modal analysis of small surface emitting lasers with a selectively oxidized waveguide," *Appl. Phys. Lett.*, vol. 66, p. 2616, 1995.

[25] T. Rössler, R. A. Indik, G. K. Harkness, J. V. Moloney, and C. Z. Ning, "Modeling the interplay of thermal effects and transverse modes behavior in native-oxide-confined vertical-cavity surface-emitting lasers," *Phys. Rev. A*, vol. 58, pp. 3279–3292, 1998.

[26] M. Glick, F. K. Reinhart, and D. Martin, "Linear electro-optic effect: Comparison of GaAa/AlGaAs multi-quantum-well heterostructures with an AlGaAs solid solution at 1.1523 μm," *J. Appl. Phys.*, vol. 63, p. 5877, 1988.

[27] K. Panajotov, B. Nagler, G. Verschaffelt, A. Georgievski, H. Thienpont, J. Danckaert, and I. Veretennicoff, "Impact of in-plane anisotropic strain on the polarization behavior of vertical-cavity surface-emitting lasers," *Appl. Phys. Lett.*, vol. 77, p. 1590, 2000.
[28] J.-P. Hermier, A. Bramati, A. Z. Khoury, V. Josse, E. Giacobino, P. Schnitzer, R. Michalzik, and K. J. Ebeling, "Noise characteristics of oxide-confined vertical-cavity surface-emitting lasers," *IEEE J. Quantum Electron.*, vol. 37, pp. 87–91, 2001.
[29] P. Debernardi and G. P. Bava, "Vectorial modes in vertical-cavity surface-emitting lasers in presence of anisotropies," Phys. Stat. Sol. (a), vol. 188, no. 3, 2001, submitted for publication.
[30] L. Fratta, P. Debernardi, G. P. Bava, C. Degen, J. Kaiser, I. Fischer, and W. Elsäßer, "Spatially inhomogeneously polarized transverse modes in vertical-cavity surface-emitting lasers," Phys. Rev. A, Rap. Comm., vol. 64, no. 031803(R), pp. 1–4, 2001, to be published.

Pierluigi Debernardi was born in Casale Monferrato, Italy, in 1963. He received the degree in electronics engineering from Politecnico di Torino, Torino, Italy, in 1987.

Since 1989, he has been with with IRITI, an Institute of the Italian National Council of Research, Politecnico di Torino. His research interests are mainly in the field of the modeling of semiconductor materials and devices for optoelectronic applications, and especially III–V quantum wells, computing their optical response with coulomb effects included on the basis of the second quantization approach. He was involved in ridge waveguide laser simulation, analysis of optical bistable behavior of multiple quantum-well devices, and four-wave mixing in semiconductor oscillators and amplifiers. Recently, his research has mainly focused on microcavity lasers, photonic bandgap structures, and VCSELs modelling, considering in particular their modal properties so to compute their statical, dynamical, and noise behavior.

Gian Paolo Bava was born in Varallo Sesia, Italy, in 1937. He received the degree in electrical engineering from Politecnico di Torino, Torino, Italy, in 1961.

Since 1961, he has been with the Dipartimento di Elettronica, Politecnico di Torino, as a Full Professor of Microwave Techniques since 1976. His research activities have been concerned successively with traveling-wave tubes for satellite applications, microwave semiconductor devices (Mesfet, Gunn effect, etc.) and amplifiers both regarding simulation and characterization, and integrated optics and optoelectronics, mainly with reference to parametric oscillators and semiconductor lasers. Recently, his interests have focused on the modeling of semiconductor materials and devices, most recently including the modeling of VCSELs.

Christian Degen was born in Neuwied, Germany, in 1970. He received the degree in physics in 1997 for work on surface-emitting second-harmonic generation in semiconductor waveguides and the Ph.D. degree in 2001 for an experimental work on the mechanisms that determine the transverse mode formation in oxide-confined VCSELs, both from from Darmstadt University of Technology, Darmstadt, Germany.

His interests include spectral, spatial, and polarization effects, as well as quantum-noise properties in semiconductor lasers. Currently, he is a Development Engineer for Infineon Technologies, Munich, Germany, where his attention is focused on the detailed characterization of VCSELs for high-bit-rate optical data transmission.

Ingo Fischer was born in Marburg, Germany, in 1966. He received the diploma degree in 1992 and the Ph.D. degree in 1995, both in physics from the Philipps University, Marburg, Germany.

In 1995, he joined the Institute of Applied Physics, Darmstadt University of Technology, Darmstadt, Germany, where his research activities are centered around spatial, spectral, and dynamical emission properties of semiconductor lasers. He is also engaged in studies on nonlinear dynamics, synchronization of coupled lasers, VCSEL emission, high-power laser emission, phase conjugation, and femtosecond spectroscopy. Research stays have included AFRL/DELO, Albuquerque, NM, in 1999, and ATR, Kyoto, Japan, in 1999 and 2000.

Dr. Fischer received the Research Prize of the Adolf–Messer Foundation in 2000.

Wolfgang Elsäßer (M'94–SM'97) was born in Pforzheim, Germany, in 1954. He received the degree in physics from the Technical University, Karlsruhe, Germany, in 1980, the Ph.D. degree in physics from the University of Stuttgart, Stuttgart, Germany, in 1984, and the Habilitation degree in experimental physics from Philipps University, Marburg, Germany, in 1991.

From 1981 to 1985, he was with the Max–Planck Institute for Solid State Research, Stuttgart, Germany. From 1985 to 1995, he was with with Philipps University. Since 1995, he has been a Full Professor at the Institute for Applied Physics, Technical University (Darmstadt University of Technology), Darmstadt, Germany. In 1992, he spent a sabbatical at the Ecole Nationale Superieure des Telecommunications, Paris, France. In 1990, 1996, 1999, and 2000, he was with Trinity College, Dublin, Ireland, on a research stay. His areas of research interest include nonlinear dynamics, quantum optics of semiconductor lasers, squeezing, quantum metrology, phase conjugation and multi-wave mixing, nonlinear optics in passive semiconductor waveguide structures, picosecond pulse generation and mode locking of semiconductor lasers, ultrashort pulse dynamics, and spectroscopy in lasers and amplifiers.

Dr. Elsaesser is Member of the German Physical Society (DPG). He was awarded the Otto-Hahn-Medal (1985), the Werner-von-Siemens-Medal (1985), the Rudolf-Kaiser Prize (1991), and the IEE J. J. Thomson Premium (1995).